Monthly Notices
of the
ROYAL ASTRONOMICAL SOCIETY

MNRAS **487,** 5862–5873 (2019)
Advance Access publication 2019 June 19

doi:10.1093/mnras/stz1679

The star formation history of the Sculptor dwarf spheroidal galaxy

M. Bettinelli ,[1,2,3]★ S. L. Hidalgo,[1,2]★ S. Cassisi,[1,4,5]★ A. Aparicio,[1,2] G. Piotto,[3,6] F. Valdes[7] and A. R. Walker[8]

[1]*Instituto de Astrofisica de Canarias, Vìa Làctea S/N, E-38200 La Laguna, Tenerife, Spain*
[2]*Department of Astrophysics, University of La Laguna, E-38200 La Laguna, Tenerife, Canary Islands, Spain*
[3]*Dipartimento di Fisica e Astronomia 'Galileo Galilei', Università degli Studi di Padova, Vicolo dell'Osservatorio 3, I-35122 Padova, Italy*
[4]*INAF – Osservatorio Astronomico d'Abruzzo, Via M. Maggini, I-64100 Teramo, Italy*
[5]*INFN - Sezione di Pisa, Largo Pontecorvo 3, 56127 Pisa, Italy*
[6]*INAF – Osservatorio Astronomico di Padova, Vicolo dell'Osservatorio 5, I-35122 Padova, Italy*
[7]*National Optical Astronomy Observatory, P.O. Box 26732, Tucson, AZ 85719, USA*
[8]*Cerro Tololo Inter-American Observatory, National Optical Astronomy Observatory, Casilla 603, La Serena, Chile*

Accepted 2019 June 15. Received 2019 June 10; in original form 2018 July 30

ABSTRACT

We present the star formation history (SFH) of the Sculptor dwarf spheroidal galaxy based on deep *g*, *r* photometry taken with Dark Energy Camera at the Blanco telescope, focusing our analysis on the central region of the galaxy extended up to ∼3 core radii. We have investigated how the SFH changes radially, subdividing the sampled area into four regions, and have detected a clear trend of star formation. All the SFHs show a single episode of star formation, with the innermost region presenting a longer period of star formation of ∼1.5 Gyr and for the outermost region the main period of star formation is confined to ∼0.5 Gyr. We observe a gradient in the mean age which is found to increase going towards the outer regions. These results suggest that Sculptor continued forming stars after the reionization epoch in its central part, while in the peripheral region, the majority of stars probably formed during the reionization epoch and soon after its end. From our analysis, Sculptor cannot be considered strictly as a fossil of the reionization epoch.

Key words: galaxies: dwarf – galaxies: individual: (Sculptor) – Local Group – early Universe.

1 INTRODUCTION

The first dwarf spheroidal (dSph) galaxy to be discovered early in the last century by Shapley (1938) is Sculptor. Since then, many other dwarf galaxies satellites of the MW have been discovered. Historically, Sculptor, with Fornax, Leo I, Leo II, Draco, Ursa Minor, Carina, and Sextans, is considered as the prototypical dSph galaxy (McConnachie 2012); these galaxies are defined *early-type dwarf galaxies* (van den Bergh 1999;Tolstoy, Hill & Tosi 2009) thus systems with a total luminosity of $M_B > -14$, characterized by low optical surface brightness ($V \sim 22 - 26$ mag arcsec^{-2}), no nucleus and poor gas content (Gallagher & Wyse 1994). Despite these similarities, almost all dwarfs disclose their own peculiarities in the properties of their stellar populations such as in the star formation history (SFH), chemical patterns, stellar variable populations, and dark matter content.

Sculptor has been studied in depth since its discovery, photometrically, spectroscopically and in the radio wavelengths, in order to detect the presence of neutral hydrogen (HI). Sculptor was found to be embedded in two HI clouds symmetrically distributed respect to the optical centre (Carignan et al. 1998;Bouchard, Carignan & Mashchenko 2003;Piatek et al. 2006). This finding is very important since Sculptor is the only dSph galaxy known to have retained this gas. The major parameters relative to this system are listed in Table 1.

Even though, at a first sight, the morphology of its colour–magnitude diagram (CMD) appears quite simple, the analysis of its stellar populations and SFH is not trivial, as will be shown in the present analysis. The published CMDs do not show a strong intermediate-age population, while the large red giant branch (RGB) spread suggests the presence of internal age or abundances variations (Da Costa 1984).

Monkiewicz et al. (1999) observed a small region of ∼2 arcmin^2 located 14.1 arcmin from the centre of Sculptor, using the Wide-Field Planetary Camera 2 aboard the *Hubble Space Telescope*. The resulting CMD reaches 3 mag below the oldest main-sequence (MS) turn-off (TO) and it resembles the stellar population of the earliest globular clusters. In the same year, Hurley-Keller, Mateo & Grebel (1999) published a wide field deep CMD based on data taken with Big Throughput Camera at the Cerro Tololo Inter-American Observatory (CTIO) 4 m telescope. The quality of this CMD, in terms of its combination of depth and area, is unprecedented.

By means of a study of the chemical, kinematic, and spatial distribution of its stellar populations on a region extended 40

★ E-mail: mbettine@iac.es (MB); shidalgo@iac.es (SLH); santi.cassisi@inaf.it (SC)

Table 1. The main properties of the Sculptor dSph.

Quantity	Value	References[a]
RA, α (J2000.0)	$1^h00^m09^s.4$	(1)
Dec., δ (J2000.0)	$-33^\circ\ 42'\ 33.0''$	(1)
Galactic longitude, l (°)	287.53	(1)
Galactic latitude, b (°)	−83.16	(1)
Galactocentric distance (kpc)	86 ± 5	(2)
Heliocentric velocity (km s^{-1})	109.9 ± 1.4	(3)
Ellipticity, e	0.32 ± 0.03	(4)
Position angle (°)	99 ± 1	(4)
Core radius (arcmin)	5.8 ± 1.6	(4)
Tidal radius (arcmin)	76.5 ± 5.0	(4)
Luminosity, L_V ($L_\odot$)	(2.03 ± 0.79) × 10^6	(5)
Absolute magnitude,M_V	− 10.94 ± 0.58	(5)
Total mass, ($M_\odot$)	(3.1 ± 0.2) × 10^7	(5)
Mass to light ratio, $M_\odot/L_\odot$	15.4 ± 6.9	(5)

[a](1) de Vaucouleurs et al. (1991); (2) Pietrzyński et al. (2008); (3) Queloz, Dubath & Pasquini (1995); (4) Irwin & Hatzidimitriou (1995); (5) Łokas (2009).

arcmin from the centre of Sculptor, Tolstoy et al. (2004) discovered the presence of two distinct ancient stellar components (both ≥10 Gyr). These two stellar components are characterized by different metallicities (one metal rich −0.9 > [Fe/H] > −1, 7, one metal poor −1.7 > [Fe/H] > −2.8), distributions (the metal-rich is more centrally concentrated, while the metal-poor is spatially extended), and velocity dispersions ($\sigma_{\text{metal-rich}} = 7 \pm 1$ km s^{-1} and $\sigma_{\text{metal-poor}} = 11 \pm 1$ km s^{-1}). Battaglia et al. (2008) confirmed the above results (on a radial distance of ∼1 deg centred on the galaxy), moreover they measured a velocity gradient of ∼8 km s^{-1} deg^{-1} along the projected major axis of Sculptor, likely due to intrinsic rotation. Also Coleman, Da Costa & Bland-Hawthorn (2005) and Westfall et al. (2006) by means of wide-field medium resolution Ca II triplet spectroscopy of RGB stars independently confirmed the presence of two distinct components. Martínez-Vázquez et al. (2016) detected the presence of a significant metallicity spread (∼2 dex) within the RR Lyrae population, which is a population older than 10 Gyr. This suggests that Sculptor underwent an efficient early chemical enrichment fast enough to be recorded by the RR Lyrae. de Boer et al. (2012) presented the SFH of Sculptor based on deep wide-field *B*, *V*, *I* photometry taken with Mosaic II camera at the CTIO 4 m Blanco telescope on an area of 1 deg^2 centred on Sculptor (de Boer et al. 2011). de Boer et al. (2012) found that Sculptor is dominated by an old (>10 Gyr) metal-poor stars, but that younger, more metal-rich populations are also present.

In the present work, we take advantage of deep, wide-field ground-based photometry for deriving the SFH of the Sculptor dSph galaxy. The article is organized as follows: in Section 2, the observations and the data reduction are described along with the derivation of the photometry. The photometric calibration and the resulting CMD of Sculptor are presented too. In Section 3, we discuss completeness tests and error simulations. In this section is also illustrated the SFH derivation procedure. In Section 4, the results are discussed. Finally, summary and conclusions are presented in Section 5.

2 OBSERVATIONS AND DATA REDUCTION

Table 2 lists all the deep, wide-field exposures in *g* and *r* filters that have been used to construct the scientific stacked images. All the data were taken with Dark Energy Camera (DECam, Flaugher et al. 2015) at the Blanco 4 m telescope at the CTIO, reduced with the NOAO Community Pipeline (Valdes, Gruendl & DES 2014) and retrieved from the NOAO Science Archive (Seaman et al. 2002). We obtained a stacked image for each filter as an average of all the scientific observations listed in Table 2 and we concentrated our analysis on the central CCDs centred on the galaxy, with a corresponding radial extension of ∼20 arcmin from the centre of Sculpor. The total exposure time is 4800 s in the *g* filter and 4500 s in the *r* filter.

The photometry on stacked images and on calibration images has been performed using the DAOPHOT/ALLSTAR suite of programs (Stetson, Davis & Crabtree 1990). We used as point spread function (PSF) a Moffat function with parameter $\beta = 2.5$ and radius of $R_{\text{PSF}} =$ 15 pixels. A linearly varying PSF with the position of the stars has been derived for each stacked image by fitting 129 stars in the *g* filter and 60 stars in the *r* filter. In order to reduce to 1 per cent the impact of the so-called brighter-fatter effect (Antilogus et al. 2014) we have chosen only stars with 5−10 K adu peak, excluding in this way the brightest stars. In order to remove poorly measured stars, and galaxies, only sources with $\sigma \leq 0.2$ and $-0.5 \leq$SHARP≤ 0.5 were considered from the output of ALLSTAR. In Fig. 1 are plotted the magnitudes and the corresponding photometric errors for each filter with the restrictions above applied.

With the two catalogues in the *g* and *r* filters in hand, we performed the match using the packages DAOMATCH and DAOMASTER (Stetson 1993). The final total catalogue, resulting from the match above, in *g* and *r* filters contains ∼96 000 stars. We performed the aperture corrections for each filter, from the comparison between aperture and PSF magnitudes, finding for the *g* filter 0.0121 mag and for the *r* filter 0.0351 mag. Then we corrected for the exposure time, in *g* filter applying $+2.5 \times \log(300)$, while in *r* filter, $+2.5 \times \log(300)$. The quantities into the parenthesis have been calculated as the average of each exposure time in each filter.

In order to calibrate the photometry derived from the stacked images for each filter we have performed a two-step calibration. The final scientific stacked images are composed among the others by a set of observations performed by Vivas (see last four rows

Table 2. A summary of the available observational data sets.

Calibration images	Filter	UT	Exposure (s)	Seeing (arcsec)	Program	PI
	g	2013/08/19	300 × 1	1.2−1.4	2013B-0325[*Scl*]	Vivas
	g	2013/08/19	120 × 9	1.2−1.4	2013B-0325[*Stripe*82]	Vivas
	r	2013/08/19	300 × 1	0.9−1.1	2013B-0325[*Scl*]	Vivas
	r	2013/08/19	120 × 7	0.9−1.1	2013B-0325[*Stripe*82]	Vivas
Scientific images	Filter	UT	Exposure (s)	Seeing (arcsec)	Program	PI
	g	2013/08/19	300 × 16	1.2−1.4	2013B-0325	Vivas
	r	2013/08/19	300 × 15	0.9−1.1	2013B-0325	Vivas

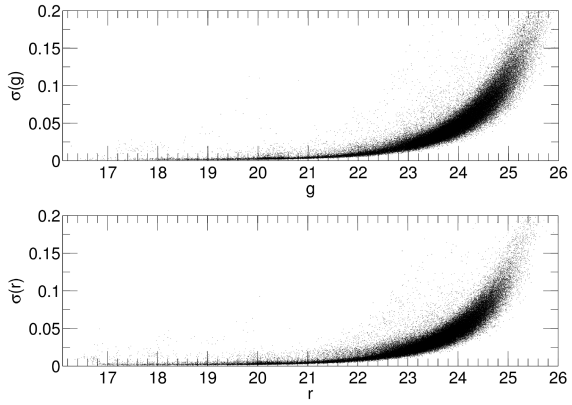

Figure 1. Calibrated magnitudes plotted against the corresponding photometric errors.

in Table 2). Thus, we first performed PSF photometry on the stacked images of Sculptor by Vivas, obtaining the catalogue in g and r filters. Then, we retrieved the PSF photometry of the single images of the standard stars observed the same night, see Stripe 82 observations in Table 2. We indentified the standard stars by using the SDSS Stripe 82 standard stars catalogue (Ivezić et al. 2007). The magnitudes of photometric standard stars has been compared to the SDSS Stripe 82 catalogue in order to obtain the extinction coefficients for that night for both filters. Knowing the extinction coeffiecients and the photometry of standard stars, we derived the equations for the standard calibration:

$$\begin{aligned} g' - g = &\quad k_g \times X_g + c_{g1} \times (g' - r') + g_0 \\ r' - r = &\quad k_r \times X_r + c_{r1} \times (g' - r') + r_0 \end{aligned} \tag{1}$$

where g', r' are the calibrated magnitudes, g, r, the observed magnitudes, k_g, k_r the airmass coeffiecients, X_g, X_r the effective airmasses, c_g, c_r, the colour therms, and g_0, r_0, the photometric zero-points. We derived the photometric solution using a polynomial regression model for the three independent variables. The root-mean-square error associated to this transformation are 0.0158 mag in g filter and 0.0201 mag in r filter, hence indicating a good match with the standard system.

Using the system of equations above we applied the calibration to the Vivas' catalogue. In this way these stars can serve as local standards. Then, from the comparison between the magnitudes of the local standards with the full catalogue, we obtained the equations to calibrate the full catalogue:

$$\begin{aligned} g' - g = &\quad c_{g2} \times (g' - r') + z_g \\ r' - r = &\quad c_{r2} \times (g' - r') + z_r \end{aligned} \tag{2}$$

where c_{g2}, c_{r2} are the colour therms and z_g, z_r, the photometric zero-points. In Table 3 are listed all the coefficients relative to the two obtained photometric tranformations, with the corresponding errors.

2.1 The colour–magnitude diagram

The resulting CMD of Sculptor extends ∼2 mag below the MSTO (see Fig. 2), thus allowing us to extract the information relative to star formation also for the earliest epochs. Fig. 2 shows the resulting CMD, corrected by reddening ($A_g = 0.06$ and $A_r = 0.042$, Schlegel, Finkbeiner & Davis 1998; Schlafly & Finkbeiner 2011), with over-plotted four BaSTI isochrones (Pietrinferni et al. 2004) adopting as distance modulus $(m - M)_0 = 19.57$ (Menzies et al. 2011). The

Table 3. Airmass coefficients, colour therms, and photometric zero-points adopted for the calibration. The associated errors are also listed.

Parameter	Values
k_g	-0.1514 ± 0.0064
c_{g1}	0.1157 ± 0.0029
g_0	25.4106 ± 0.0083
k_r	-0.1264 ± 0.0082
c_{r1}	0.0918 ± 0.0037
r_0	25.5771 ± 0.0106
z_g	25.3062 ± 0.0008
c_{g2}	0.1113 ± 0.0014
z_r	25.4677 ± 0.0007
c_{r2}	0.0902 ± 0.0012

MS is well matched by isochrones of [Fe/H] = −1.7 and −1.5 and an age of about 13 Gyr. The RGB locus is very broad showing a spread in [Fe/H] between −2.2 and −1.3. Actually, an exhaustive spectroscopic analysis of the RGB has shown that this dwarf seems to have a significant spread that varies with position on the RGB (de Boer et al. 2011). In the obtained CMD, there is a region ($-0.3 \lesssim (g - r)_0 \lesssim 0.08$, $21.5 \lesssim r_0 \lesssim 23.2$) that appears to be populated by blue straggler stars (BSS, Mapelli et al. 2009; Monelli et al. 2012).

3 DERIVATION OF THE SFH

The SFH of Sculptor has been derived following the prescriptions of Aparicio & Hidalgo (2009) and Hidalgo et al. (2011). The star formation rate (SFR) as a function of time and the age–metallicity relation have thus been computed. We made use of IAC-Star (Aparicio & Gallart 2004) for the synthetic CMDs (sCMDs) computation. IAC-pop (Aparicio & Hidalgo 2009), which is the key algorithm for solving for the best parametrization of the SFH. Finally, for sampling the parameter space, creating input data to IAC-pop and averaging solutions, MinnIAC (Hidalgo et al. 2011) was used.

Using IAC-star with the BaSTI stellar evolutionary library, we created an sCMD, which is used to derive the stellar properties of Sculptor. It is composed by 5×10^6 stars, with a constant SFR from 0 to 13.5 Gyr and a flat metallicity distribution in the interval $0.0001 \leq Z \leq 0.002$ for all ages. The Kirby et al. (2011) metallicity distribution function (MDF) has been used as a template to determine this metallicity interval. We adopted the bolometric corrections for the SLOAN photometric systems provided by Pietrinferni et al. (2004), based on the model atmospheres by Castelli & Kurucz (1993). A Kroupa (2002) initial mass function has been adopted and a population of binary stars has also been simulated. For this case, we assumed $f = 0.3$ for the fraction of binary stars and $q_{min} = 0.5$ as the minimum secondary to primary stellar mass ratio q with a flat distribution for this last parameter. An accurate modelling of observational effects is a crucial step in the obtainment of a realistic model CMD to be compared with the real data (Aparicio & Gallart 1995). As outlined in Hidalgo et al. (2011), 5×10^6 artificial stars has been injected in each stacked image along an uniform grid, with a separation of at least $2 \times R_{PSF} + 1$ pixels between the centroids of each of them. Then, the photometry has been performed again on these stacked images, using the same configuration as done for the original ones. Magnitude values of the injected artificial stars have been generated according to $-1.25 \leq (g - r) \leq 2$ and $16.75 \leq g, r \leq 26$ in order to cover the entire range of luminosity and colour of the observed CMD (oCMD) (see Fig. 2). Since the the TO region ($22 \leq g, r \leq 26$) is of highest interest for

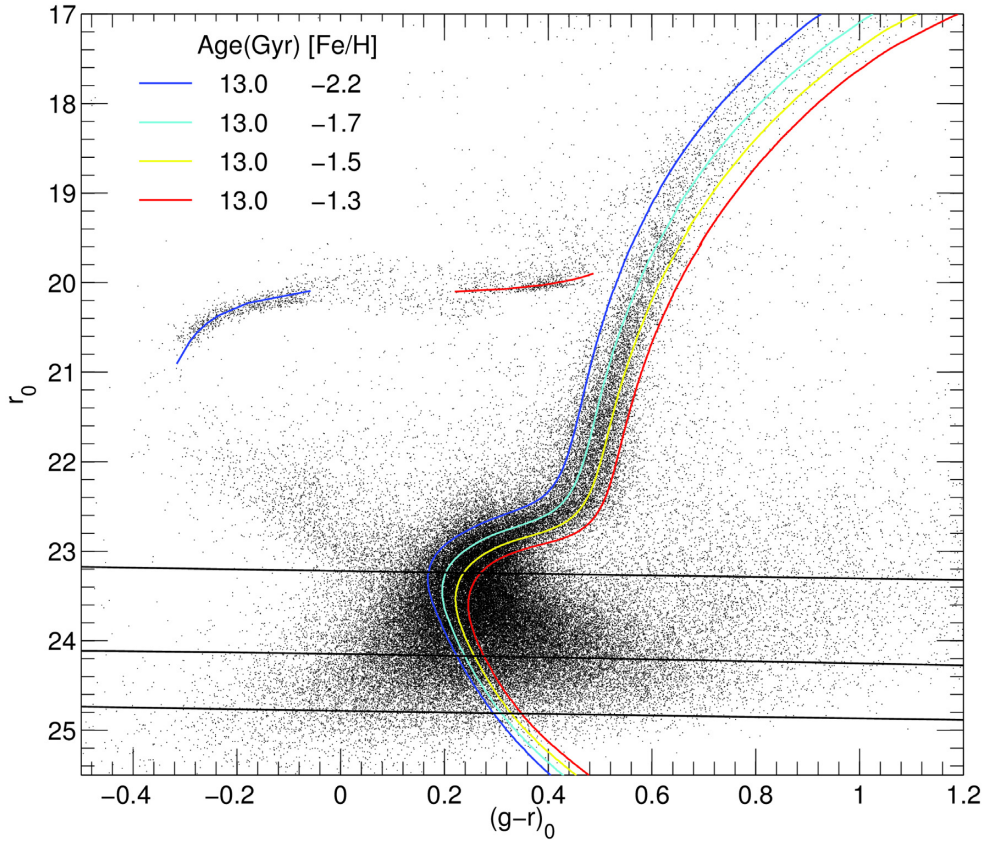

Figure 2. Observed CMD of Sculptor dSph. Four BaSTI isochrones have been superimposed on the CMD, see the labels for details. The BHB and RHB are fitted with a zero-age horizontal branch (ZAHB) of [Fe/H] = −2.2 and −1.3, respectively (solid blue and red lines in the electronic version). Completeness levels are overplotted as black lines for values corresponding to 90 per cent, 75 per cent, and 50 per cent.

the derivation of the SFH, 3.5×10^6 stars have been injected in this magnitude range, while, 1×10^6, have been generated in the RGB region ($19 \leq g, r \leq 22$). Finally, 0.5×10^6 artificial stars have been injected in the upper part of the CMD ($16.75 \leq g, r \leq 19$). The results of the completeness tests for each filter are shown in Fig. 3.

In order to measure the completeness level, the ratio between the number of the recovered artificial stars and the totality of injected ones in each colour and magnitude interval has been calculated. In Fig. 2, the 50 per cent, 75 per cent, and 90 per cent completeness levels are overplotted on the CMD of Sculpor. Moreover, the position on the image of each artificial star, along with the injected magnitude $m_{\rm inj}$ and the recovered one $m_{\rm rec}$, have been recorded in order to simulate the observational effects, see Hidalgo et al. (2011) for a detailed description of the procedure. Fig. 4 shows the sCMD accounting for the observational effects simulation.

To obtain the SFH, the sCMD has been subdivided into simple stellar populations (SSPs) and the resulting star distributions have been compared with that of the oCMD. The sampling of the sCMD into SSPs has been performed binning it in age and metallicity. For the age, intervals of 2 Gyr for the first 8 Gyr have been chosen and a smaller one, of 0.5 Gyr, for the last interval between 8 and 13.5 Gyr, since higher resolution is necessary to well characterize the earliest SFH phase. For the metallicity, we have adopted the following bins: $(0.01,\ 0.1,\ 0.3,\ 0.5,\ 1,\ 2) \times 10^{-3}$. Wider intervals have been chosen for higher Z values.

To sample the oCMD and the sCMD, *bundles* have been defined, i.e. macroregions which identify main features of the CMDs, as shown in Fig. 4.

Each *bundle* has a weight on the solution, given by the number of boxes of fixed size in colour and magnitude defined in them. More boxes are present in a *bundle*, the larger will be its weight on the resulting SFH. Table 4 shows the weight of each bundle in the solution.

The dependence of the resulting SFH on the CMDs sampling parameters has been taken into account obtaining 24 solutions varying the CMD binning within each bundle and the SSPs sampling. In particular, we have shifted by a 30 per cent the age and metallicity in a total of 12 combinations of SSPs, each one sampled with two slightly different combinations of boxes distribution in the bundles. Moreover, the effect of uncertainties in the distance modulus, reddening, and photometric calibration, has been mitigated shifting the oCMD 25 times along a regular grid with nodes in colour $\Delta(g-r) = [-0.1, -0.05,\ 0,\ 0.05,\ 0.1]$ and magnitude $\Delta r = [-0.2, -0.1,\ 0,\ 0.1,\ 0.2]$. For each node 24 solutions have been calculated as described above, obtaining a total of 600 solutions. A mean solution $\overline{\psi}$ and its $\overline{\chi^2_\nu}$ have been also calculated for each node. The $\overline{\psi}$ have been obtained by using a boxcar of width 0.5 Gyr and step 0.1 Gyr for t and width 0.00025 and step 0.00005 for Z. In this way 25 different $\overline{\chi^2_\nu}$ have been obtained, the best solution was then selected as the one with the lowest value. In this particular case, the best solution is the one corresponding to a shift of −0.05 mag in colour and no shift in r magnitude.

For an extensive description of the five bundles adopted and how we performed the minimization of the solution on the CMDs sampling parameters we refer to Hidalgo et al. (2011, see also Bettinelli et al. 2018).

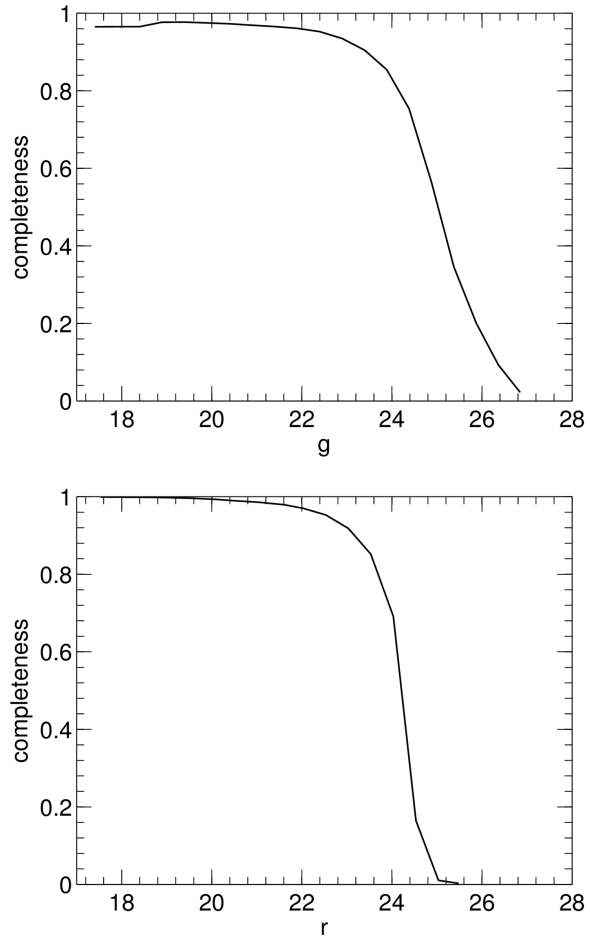

Figure 3. Results of the completeness tests as a function of g (upper panel) and r (lower panel) filter in 0.5 mag bins.

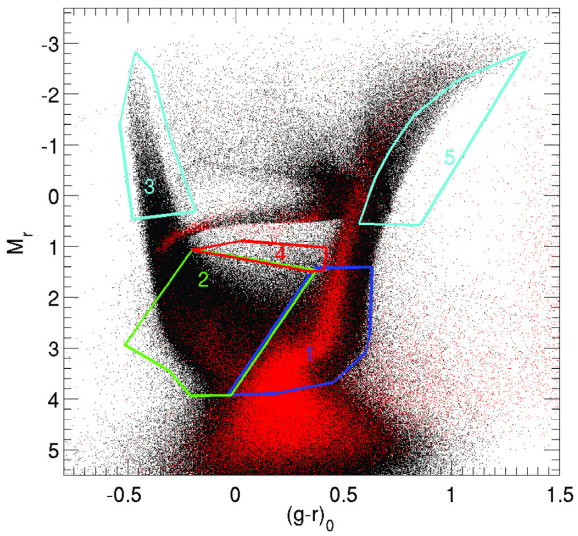

Figure 4. sCMD with the simulated observational effects (black). The observed CMD is also shown (red). Regions numbered from 1 to 5 are the adopted *bundles*, see the text for details.

3.1 The global SFH of Sculptor

Fig. 5 shows the SFR as a function of time, $\psi(t)$, the age–metallicity relation, $Z(t)$, and the cumulative mass function for Sculptor. The

Table 4. Box sizes in each bundle that sample the observed CMD.

Bundle number	Δcol	Δmag	Boxes
1	0.025	0.125	1020
2	0.1	0.205	150
3	0.1	0.23	30
4	0.1	0.23	3
5	1.5	0.67	1

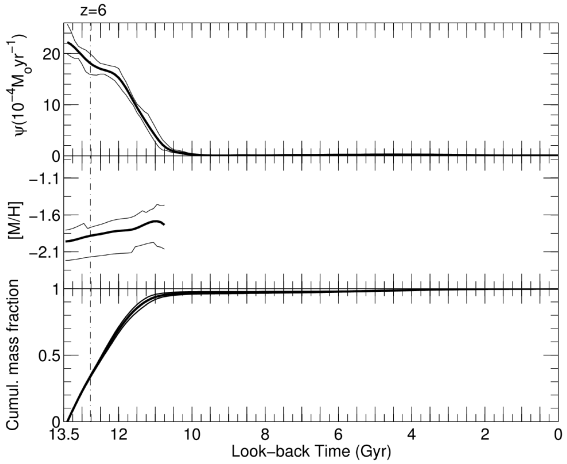

Figure 5. Results of the Sculptor SFH. Top panel: SFH as a function of time ($\psi(t)$). Middle panel: metallicity of the system as a function of the time. Lower panel: cumulative mass fraction as a function of the time. 1σ uncertainties have been drawn as thin lines.

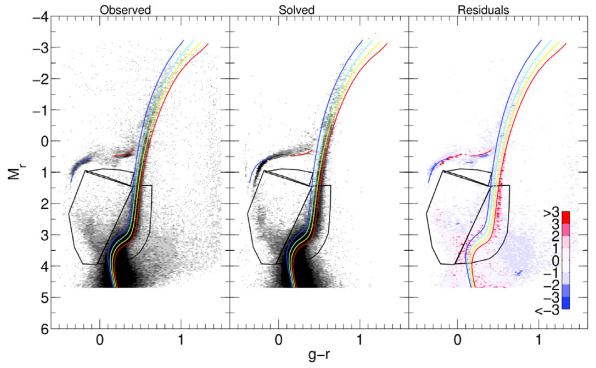

Figure 6. Left-hand panel: oCMD Hess diagram. Grey levels are proportional to the density of stars. A factor of 2 in density exists between each two successive grey levels. The single dots are shown where the density is less than 2 stars per $(0.02)^2$ mag. Middle panel: best solution CMD Hess diagram. Right-hand panel: residuals CMD Hess diagram in units of Poisson uncertainties. Values of $\sigma < 0$ are found when the oCMD contains more star than the best solution CMD. The same isochrones as in Fig. 2 are overplotted. The most relevant *bundles* used are also shown.

age resolution of our derived SFH indicates that Sculptor has experienced a single event of star formation limited to the first ∼2 Gyr after big bang, producing ∼70 per cent of its mass about 12 Gyr ago. The mean metallicity retrieved is [Fe/H] ∼ −1.8. In Fig. 6, the Hess diagrams of the oCMD (left-hand panel) and the best solution CMD (middle panel) are shown. The residuals diagram, with values expressed in units of Poisson error, is also shown in

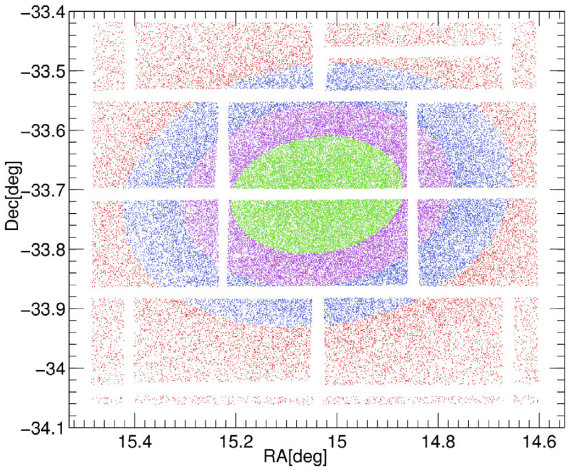

Figure 7. Stellar spatial distribution. The ellipse major axis are in the intervals $a \leq 8.59$ arcmin for green points; $8.59 < a \leq 13.41$ arcmin for magenta points; $13.41 < a \leq 19.35$ arcmin for blue points; and $a \geq 19.35$ for red points. The region of the core radius is well represented by the innermost elliptical region (green points).

the right-hand panel. It can be noted that there is good agreement between oCMD and the best solution CMD in the metallicity range $-2.2 <$ [Fe/H] < -1.3, where the bulk of the distribution of stars lies. Out of this range, the residuals progressively worsen indicating a relative excess of model with respect to the observed distribution. For a stellar population of age fixed at 13 Gyr old, the bad residuals in the blue region of the MS would show an overestimation of the more metal-poor stars, while the bad residuals in the red side of the RGB would be produced by an overestimation of the metal-rich stars. This effect could be due, at least in part, to some still-present shortcomings in the available colour–$T_{\rm eff}$ relations used for transferring the stellar models from the theoretical plane to the observational ones.

Table 5. Ratios between the number of stars in the RHB, BHB, and the spur region in respect to the RGB.

Region	RHB/RGB	BHB/RGB	spur/RGB
1	0.51	0.50	0.55
2	0.32	0.47	0.38
3	0.16	0.56	0.27
4	0.11	0.52	0.25

3.2 The radial SFH of Sculptor

To investigate whether a radial gradient of stellar populations exists in Sculptor, we derived the SFH by dividing the sampled area into four elliptical regions with delimiting major axis of 8.59, 13.41, 19.35, and 39.46 arcmin (see Fig. 7). The centre assumed for the analysis is coincident with the one tabulated by Shapley (1938) in J2000.0 coordinates (15.03898, −33.70903). The position angle adopted is $\theta = 99$ and ellipticity 0.32 (Irwin & Hatzidimitriou 1995). The major axes have been fixed in order to have 24 000 stars in each elliptical region for statistical consistency. Fig. 8 shows the CMDs for each elliptical region in which the galaxy has been divided.

For each region the SFH has been derived in the same ways for the global one but using in each case the corresponding oCMD (see Fig. 8).

Regarding the morphological changes connected to stellar populations variations, it is remarkable how the horizontal branch (HB) changes with distance: a populated red HB (RHB) is present in the centre, but it seems to be less populated moving outwards, while blue HB (BHB) stars seem constant along all the radial distance. This suggests the presence of an extended old metal-poor stellar population and a more centrally concentrated old more metal-rich stellar population.

In order to obtain a deeper insight on this effect, we calculated the ratios between the number of stars in the RHB, BHB, and the so-called *spur* (Hurley-Keller et al. 1999) region in respect to the RGB region indicated in Fig. 8. In Table 5, we report these ratios. They

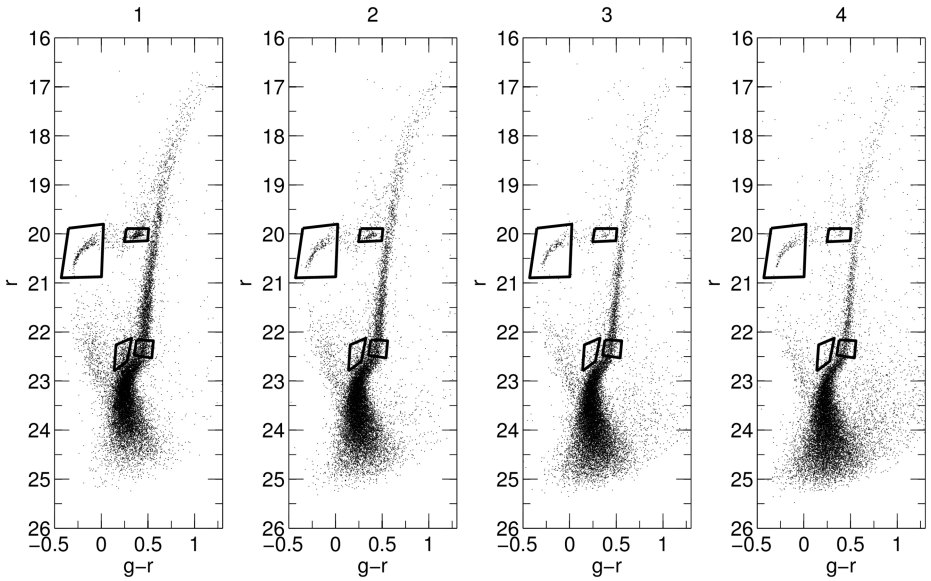

Figure 8. From left to right CMDs of Sculptor from the innermost elliptical region to the outer. Region 1 refers to the elliptical area within the major axis $a \leq 8.60$ arcmin, region 2 to the major axis $8.60 \leq a \leq 13.42$ arcmin, region 3 to the major axis $13.42 \leq a \leq 19.35$ arcmin, and region 4 to the major axis $19.35 \leq a \leq 39.46$ arcmin. On the CMDs are drawn boxes indicating the region of the BHB, RHB, and the spur region, near the MS. A box is indicated at the base of the RGB, see the text for details.

indicate that effectively RHB stars are more centrally concentrated while BHB stars more extended. This fact has been already shown in Tolstoy et al. (2004). The RGB seems to narrow when moving from region 1 to 4, indicating a clear change in stellar populations. In Fig. 8, we also indicate a box that extends from the MS TO region and is located between the canonical BS region and the SGB, which englobes the *spur*, a feature firstly identified in Hurley-Keller et al. (1999). The same feature is visible in the data presented in this work and it is interesting to note that this feature becomes weaker with the distance from the centre of the galaxy. In particular, from the calculated ratios it appears that also the *spur* is more centrally concentrated, but at a lower extent, when compared to the RHB.

In Fig. 9, we show the resulting SFHs (upper panels), the metallicy as a function of time (middle panels), and the cumulative mass fraction (lower panels) for all the four regions, and in Fig. 10, the corresponding Hess diagrams of the oCMD (left-hand panel), the best solution CMD (middle panel), and the residuals (right-hand panel) are plotted. In each region the star formation is consistent, within our age resolution, with a single burst of star formation. From Fig. 9, it is appreciable that the duration of star formation is shorter going outwards and we will constrain it for each case subsequently. Within errors we have not detected any metallicity gradient. Also the mean ages, within 1σ are consistent for the inner three regions except region 4 since the measured values are: 12.05 ± 0.13, 12.07 ± 0.13, 12.23 ± 0.13, and 12.45 ± 0.14 Gyr. By inspecting Fig. 9, it can be noted that there is a trend of the SFH with distance that involves also the three innermost regions. This suggests that a population gradient is present in Sculptor.

3.3 Constraining the duration of the main SFH burst

It is known that observational effects tend to broaden the main features of the SFH, mostly those reflecting the oldest episodes of star formation (Aparicio et al. 2016). To investigate this effect in the radial SFH, we have followed the procedure outlined in Hidalgo et al. (2011), to see if hints of different time-scales of star formation are detectable. For this test, we derived the SFHs for a number of mock stellar populations in the same way as for observational data adopting for each radial region the corresponding model which accounts for the local photometric errors of the region under consideration. The mock stellar populations are characterized by an increasing age width all starting 13.5 Gyr ago. Even though the peak is situated at ∼12.8 Gyr in three of the four regions, we use the oldest age so that the duration of the SFH obtained is a limit since it is expected a lower difference between the size of the injected and recovered SFH at younger ages. The duration of each burst, in terms of full width at half maximum (FWHM_{in}), has been chosen to be: 0.25, 0.5, 0.75, 1, 1.5, and 2 Gyr. Metallicity has been fixed to [Fe/H] = −1.86, which is the mean metallicity recovered for Sculptor.

In Table 6, we summarize for all the regions the mean recovered $\mathrm{FWHM}_{\mathrm{rec}}$ of each mock burst.

Fitting a single Gaussian profile to each SFH of Sculptor in the four regions we estimate the following typical width for the observed $\psi(t)$ in the age range 10−13.5 Gyr: $\sigma_{1-4} = 1.54$, 1.28, 1.23, and 1.02 Gyr, which corresponds to a $\mathrm{FWHM}_{\mathrm{obs}} = 3.63$, 3.01, 2.88, and 2.39 Gyr. In Fig. 11 we have plotted, for each region, the $\mathrm{FWHM}_{\mathrm{in}}$ Gyr of the mock bursts and their associated mean recovered $\mathrm{FWHM}_{\mathrm{rec}}$. Fitting the resulting data with a quadratic polynomial we are able to constrain the period of star formation for each region. Table 7 summarizes the results, while Fig. 12 shows the constrained duration of the bulk of the star formation as a function of radius.

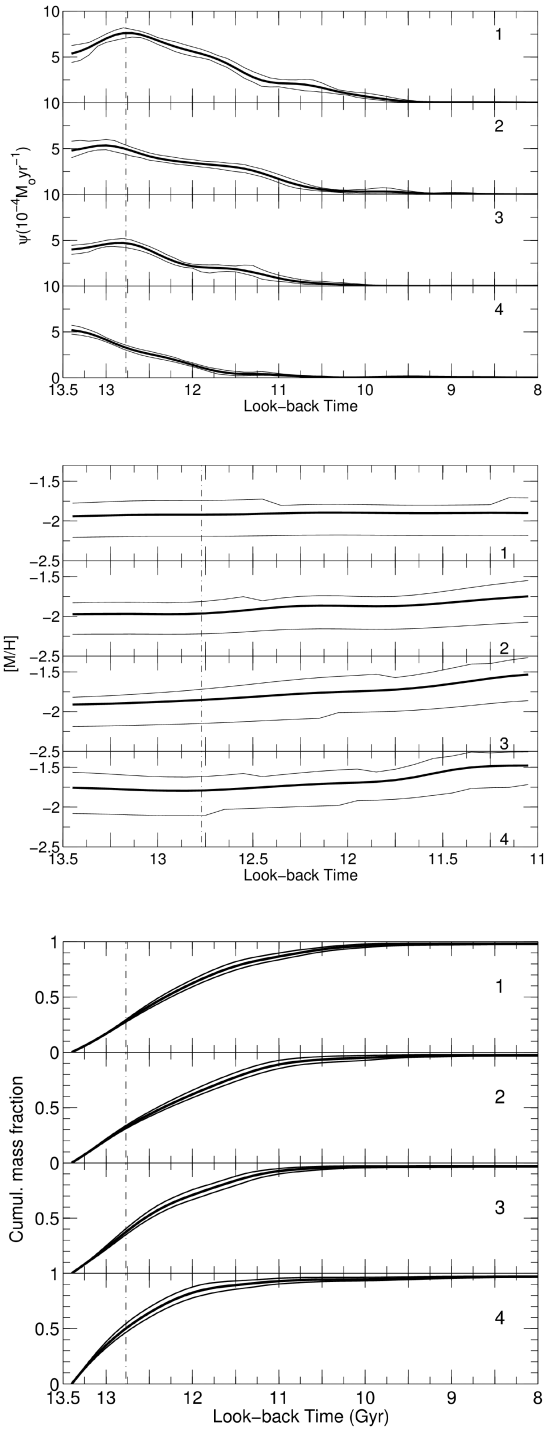

Figure 9. Results of the radial SFH (upper panels), metallicity as a function of look-back time (middle panels), and cumulative mass fraction (lower panels) for the four regions defined as in Fig. 7. Thin lines represent the uncertainties. In the panels, each region has been indicated with the corresponding number from 1 to 4.

The main star formation episode in each region decreases from the centre outwards. The star formation in region 1 lasted ∼1.5 ± 0.1 Gyr, with its peak at ∼12.8 Gyr ago. Its completion is well after the end of the epoch of reionization, which is fixed at ∼12.77 Gyr (Becker et al. 2001). The star formation episode in region 4 has been confined to ∼0.5 Gyr. Since the peak of star formation is at

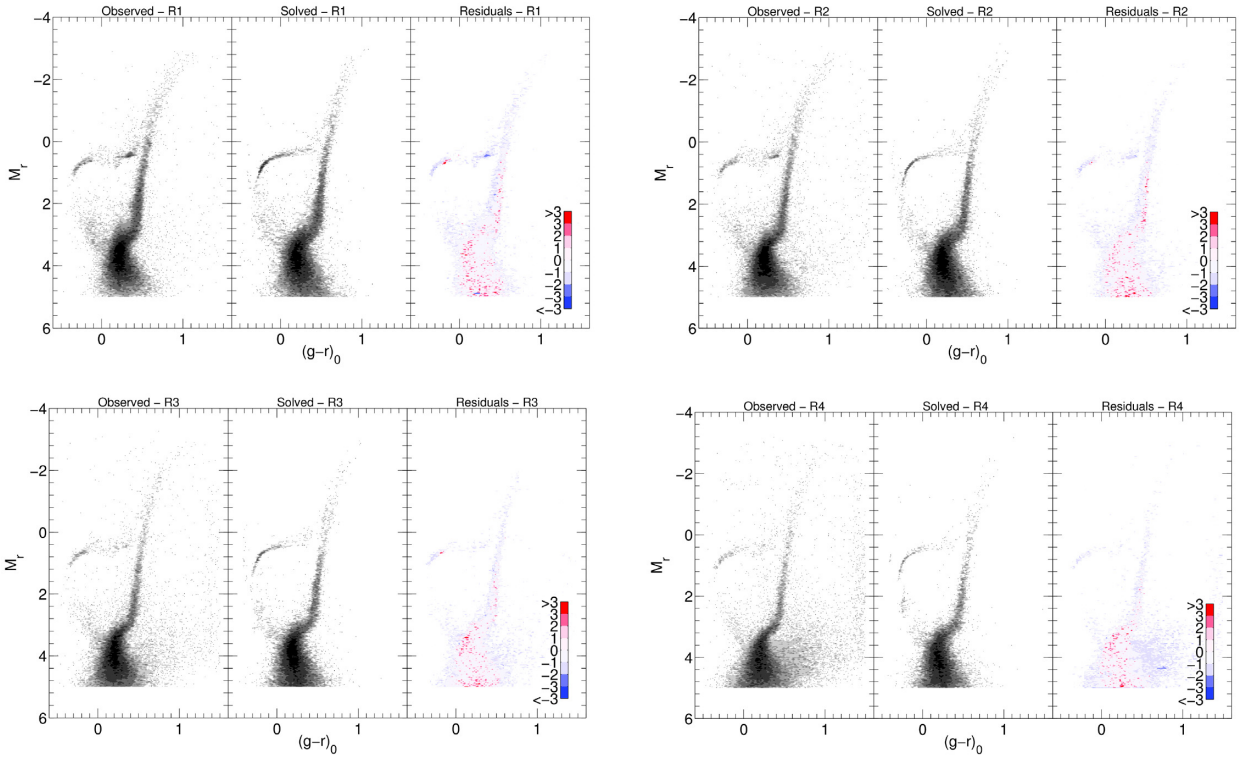

Figure 10. Upper left panel: as Fig. 6 but for stars within $a \leq 8.59$ arcmin (green points in Fig. 7). Upper right panel: same as upper left panel but for stars within $8.59 < a \leq 13.41$ (magenta points in Fig. 7). Bottom left panel: same as upper left panel but for stars within $13.41 < a \leq 19.35$ (blue points in Fig. 7). Bottom right panel: same as upper left panel but for stars within $a \geq 19.35$ (red points in Fig. 7).

Table 6. List of the recovered SFH FWHM for the mock bursts in each elliptical region.

$FWHM_{in}$	$FWHM_{rec-1}$	$FWHM_{rec-2}$	$FWHM_{rec-3}$	$FWHM_{rec-4}$
0.25	2.98	2.88	2.57	2.28
0.5	3.02	2.92	2.69	2.35
0.75	3.13	2.98	2.87	2.50
1	3.37	3.02	2.92	2.55
1.5	3.63	3.09	3.28	2.83
2	4.00	3.52	3.35	2.96

∼13.5 Gyr ago, in this region star formation terminated before the end of the epoch of reionization. This suggest that Sculptor, unlike Sextans, has continued forming stars in its inner regions, because enriched gas probably concentrated there and permitted a prolonged period of star formation.

However, the peculiarity of Sculptor is the fact that it is embedded in two symmetrical HI clouds. It is thus interesting to investigate if this neutral gas could have been ejected by supernova (SN) winds (Carignan et al. 1998). To this aim, the mechanical luminosity of the SNe released during the main star formation episode has been calculated as outlined in Hidalgo et al. (2011). We then compared this quantity, along with the value of the mass of gas of the galaxy, with the results presented in Mac Low & Ferrara (1999). This in order to infer if Sculptor had lost mass in the past and in the case the modality according to which it happened.

From the obtained SFH results that a total of $2.24 \times 10^6\,M_\odot$ of gas was converted into stars. This value has been obtained scaling the resulting SFH to the whole galaxy using the King profile of Westfall et al. (2006). Assuming a minimum progenitor mass for core-collapse SNe of $6.5\,M_\odot$ (Salaris & Cassisi 2005), a total of 3.79×10^4 SNe have been obtained. In the case of a progenitor minimum mass of $10\,M_\odot$, it results instead 2.12×10^4 SNe. For the two mass values for type II SNe listed above, we calculated a total mechanical luminosity released during the star formation episode of 1.5 Gyr of $L_w = 8.01 \times 10^{38}$ and 4.48×10^{38} erg s^{-1}, respectively. This was calculated assuming an energy release of 10^{51}erg per SN (Leitherer et al. 1999).

These values would place Sculptor in the region of blowout/mass-loss regime, from the comparison with the model results of Mac Low & Ferrara (1999) shown in their Fig. 1. In a 'blowout', the central SN explosions blow a hole through the intergalactic medium, accelerating some fraction of gas and releasing the energy of subsequent explosions without major effects on the remaining gas.

In other words, the star formation began with an initial strong burst slowed by gas loss due to SNe explosions. Later the remaining gas concentrated again in the innermost region permitting a second or more episodes of star formation. The confinement obtained for the star formation episode of region 4 is likely the record of the primordial large-scale star formation of Sculptor, which corresponds to the BHB stars that are present in each partial CMD in Fig. 8.

Knowing the radial SFHs and following the prescription in Hidalgo et al. (2013), we are able to provide some predictions about the structural properties of this dwarf, such as the core radius and the total stellar mass. We fit our results with an exponential profile, $\psi(r) = M_0 e^{-r/\alpha_\psi}$, where M_0 is the central mass density and α_ψ is the scale length.[1] For Sculptor we derived α_ψ =

[1]Radius at which mass drops by e^{-1}.

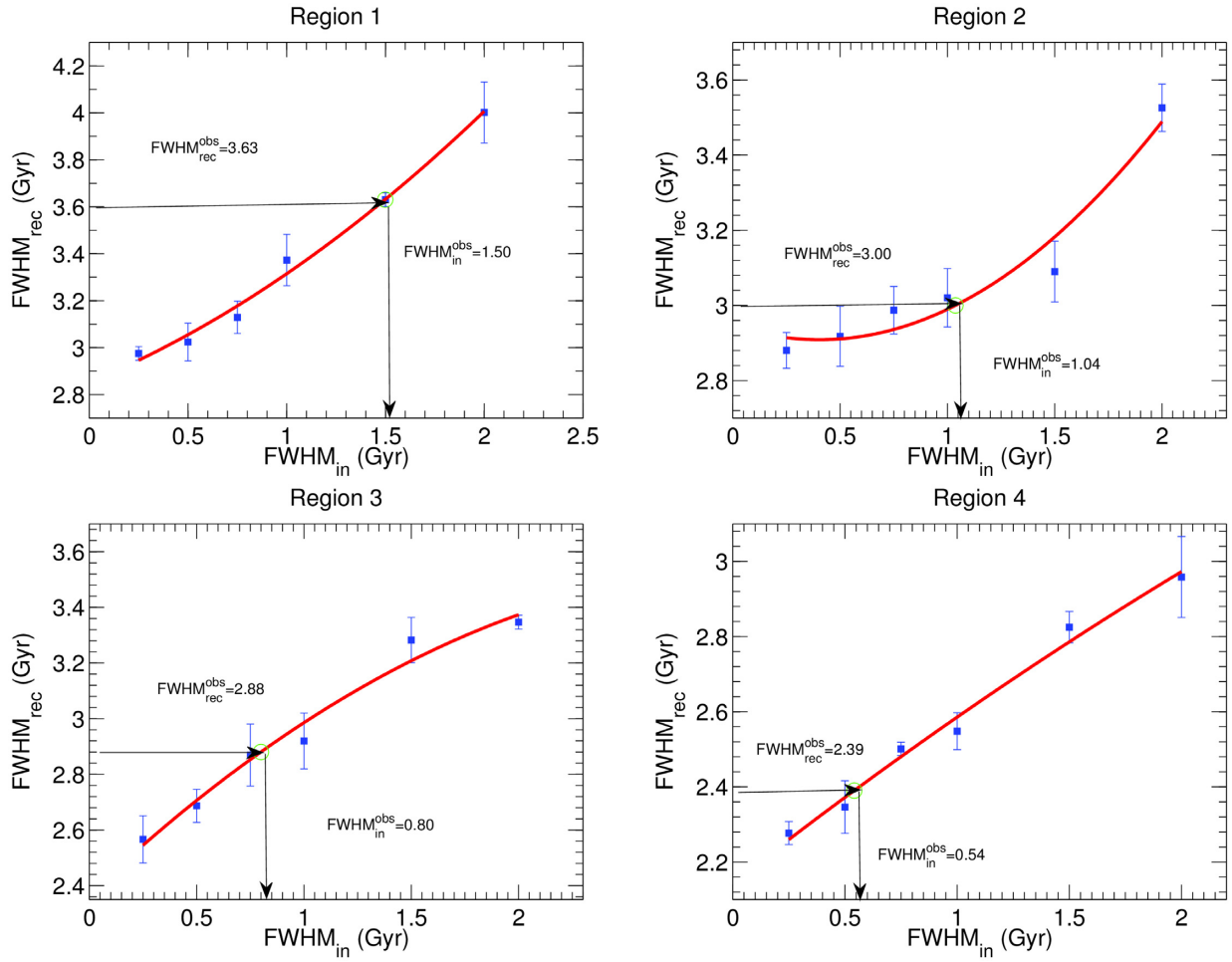

Figure 11. Burst duration confinement. Input FWHM of the mock bursts, $FWHM_{in}$, versus the recovered SFH FWHM, $FWHM_{rec}$ (blue dots). Points have been fitted with a quadratic polynomial (red line). Confinement of the star formation burst duration has been obtained by intercepting the fitting the red line (green circle) at the $FWHM_{in}$ value corresponding to the best solution SFH. Upper left panel: confinement relative to region 1, the star formation burst duration results $FWHM_{in}^{obs} \sim 1.5$ Gyr. Upper right panel: same as upper left panel but for region 2; we confine the star formation event to a value of $FWHM_{in}^{obs} \sim 1$ Gyr. Bottom left panel: same as upper left panel but for region 3; we confine the star formation event to a value of $FWHM_{in}^{obs} \sim 0.8$ Gyr. Bottom right panel: same as upper left panel but for region 4; we confine the star formation event to a value of $FWHM_{in}^{obs} \sim 0.54$ Gyr.

Table 7. Constrainment of the period of star formation for each elliptical region. $FWHM_{rec}$ refers to the real measured FWHM for each SFH, while $FWHM_{in}$ is the associated constrained burst found by means of the quadratic fit. We also provide the errors associated to $FWHM_{in}$ in the last column.

Region	$FWHM_{rec}$	$FWHM_{in}$	$\sigma FWHM_{in}$
1	3.63	1.50	0.07
2	3.01	1.04	0.07
3	2.88	0.80	0.07
4	2.39	0.54	0.05

198 ± 6 pc and a core radius $CR_\psi = 320 \pm 6$ pc. Under the assumptions that the observed field provides a good representation of the whole galaxy and the radial profile of the stellar mass density follows the same $\psi(r)$ beyond the observed radius, we integrated the exponential profile, deriving a total stellar mass of $M = (6.3 \pm 0.4) \times 10^6 M_\odot$. These values are very similar to the ones obtained for Cetus in Hidalgo et al. (2013). This fact can indicate that the two galaxies have followed similar evolutionary paths.

4 DISCUSSION

It is interesting to compare the results presented above with earlier work, such as the star formation computed by de Boer et al. (2012), who have found an extended, continuous star formation of 6−7 Gyr. Our results show that Sculptor stopped forming stars ∼11.3 Gyr ago, thus indicating a duration of ∼2.2 Gyr. The difference could be explained if we consider that our photometry is deeper that the one presented in de Boer et al. (2011) and allows us to better sample the oldest MS TO. From their radial study, de Boer et al. (2012) found that the innermost annulus (whose extension is quite similar to the one adopted in the present analysis) cannot be modelled with a single narrow burst of star formation, while, for the outer annulus of their catalogue, the recovered SFH can be well approximated to a single short burst of star formation. As de Boer et al. (2012) discussed, it is particularly challenging to properly reproduce the innermost region of Sculptor, in part for crowding effects but mostly for the complex star formation. This fact can be intuited also inspecting Fig. 8: all the features of the CMD appear more narrow going outwards. The broadening can be attributed to metallicity/age spread, thus suggesting a longer star formation in the central regions.

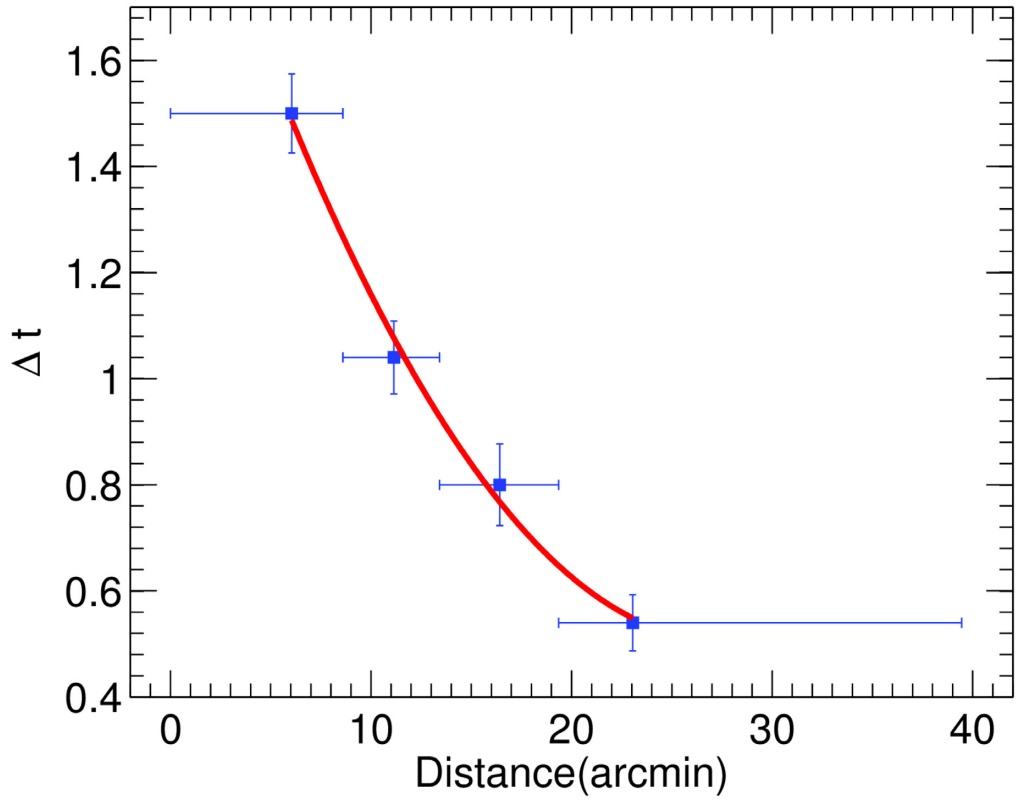

Figure 12. This figure summarizes the results achieved. The points represents the duration of the star formation in each region and a function of the distance from the centre of Scultor. The horizontal error bars refer to the radial coverage of each individual region.

From our analysis, we derived a mean metallicity for Sculptor of [Fe/H] $= -1.86$. This value is in accordance with the mean value measured by means of spectroscopy of single stars by Helmi et al. (2006) along a radius of 40 arcmin from the centre of Sculptor. Tolstoy et al. (2004) identified two distinct stellar components in Sculptor, one metal rich $-0.9 >$ [Fe/H] > -1, 7, one metal poor $-1.7 >$ [Fe/H] > -2.8. The peak of the global MDF is centred at [Fe/H] $= -1.8$. Other spectroscopic measurements have been perfomed by Kirby et al. (2009) who measured a mean metallicity of [Fe/H] $= -1.58$ and by Battaglia et al. (2008) that found a mean of [Fe/H] $= -1.56$, both sampled stars out to about 11 arcmin.

From the constraining of the SFHs radially we derived a period of $\sim$0.5 Gyr for the outermost region which is in striking agreement with the single early episode of 0.5 Gyr computed by Amorisco, Zavala & de Boer (2014) during which SNe II explosions would be sufficient to build a substantial dark matter core.

The radial gradient found in Sculptor is in agreement with outside-in scenarios of dwarf galaxy evolution, which has been found in other dwarf galaxies of the Local Group (Hidalgo et al. 2013), when these type of galaxies run out of gas on the outskirts but are able to keep forming stars in the centre for a longer period.

Finally, we would like an answer to the question if Sculptor is a fossil of the pre-reionization era, as introduced in Ricotti & Gnedin (2005): a dwarf that has experienced more than the 70 per cent of its star formation before the end of the reionization and that has a luminosity $L_{\rm V} < 10^6\,L_{\odot}$. Sculptor does not satisfies the second condition, since it has a luminosity $L_{\rm V} = (2.03 \pm 0.79) \times 10^6\,L_{\odot}$ (Łokas 2009). According to our results, region 1 is characterized by a duration of the episode of star formation of $\sim$1.5 Gyr which indicates a star formation extended also after the end of the epoch of reionization. For the outermost region 4, on the contrary, its star formation has been confined to $\sim$0.5 Gyr. There the star formation ended before or contemporaneous with the end of the epoch of reionization. From the considerations listed above, Sculptor cannot be classified strictly as a true fossil of the pre-reionization era as opposed to what we found for Sextans (Bettinelli et al. 2018). Our results suggest that Sculptor could have suffered in the past a blowout as described in Mac Low & Ferrara (1999). It is thus tempting to link this to the possible formation of the HI distribution embedding Sculptor (Carignan et al. 1998).

5 SUMMARY AND CONCLUSIONS

We have derived the global and radial SFH for the Sculptor dSph based on deep *g*, *r* photometry taken with DECam at the Blanco telescope.

The age resolution of our derived SFH indicates that Sculptor has experienced a single event of star formation limited to the first $\sim$2 Gyr after big bang, producing $\sim$70 per cent of its mass about 12 Gyr ago. The mean metallicity retrieved is [Fe/H] ~ -1.8. The retrieved metallicities are consistent with the spectroscopic measurements by Helmi et al. (2006) and Tolstoy et al. (2004). We have investigated how the SFH of Sculptor changes radially, subdividing in four regions the sampled area. In each region, the star formation is consistent, within our age resolution, with a single burst of star formation of different duration. We find that the duration of the episodes of star formation increases towards the centre and we provide the intrinsic duration of these bursts. The innermost region presents the longer period of star formation of $\sim$1.5 Gyr, in agreement with the estimate by Kirby et al. (2009) via chemo-

dynamical models, going outwards it decreases to ∼0.54 Gyr. These results suggest that Sculptor continued forming stars after the reionization epoch in its central part, while in the peripheral region the majority of stars were formed before or coincident with the end of the reionization epoch. Our results are compatible with an outside-in scenario of dwarf galaxy formation. Finally, from the calculation of the mechanical luminosity produced by SNe we can advance the hypothesis that Sculptor has suffered a 'blowout' in its early epochs that does not completely inhibit star formation. This result, together with the constraints by Ricotti & Gnedin (2005), indicates that Sculptor can not be strictly considered a fossil of the pre-reionization era.

ACKNOWLEDGEMENTS

We thank the anonymous referee for the pertinent comments and suggestions that have helped us to improve this paper. MB, SLH, SC, AA, and GP acknowledge support from the Spanish Ministry of Economy and Competitiveness (MINECO) under grant AYA2013-42781.

This research uses services or data provided by the Science Data Archive at NOAO. NOAO is operated by the Association of Universities for Research in Astronomy (AURA), Inc. under a cooperative agreement with the National Science Foundation. This project used data obtained with the DECam, which was constructed by the Dark Energy Survey (DES) collaboration. Funding for the DES Projects has been provided by the U.S. Department of Energy, the U.S. National Science Foundation, the Ministry of Science and Education of Spain, the Science and Technology Facilities Council of the United Kingdom, the Higher Education Funding Council for England, the National Center for Supercomputing Applications at the University of Illinois at Urbana-Champaign, the Kavli Institute of Cosmological Physics at the University of Chicago, the Center for Cosmology and Astro-Particle Physics at the Ohio State University, the Mitchell Institute for Fundamental Physics and Astronomy at Texas A&M University, Financiadora de Estudos e Projetos, Fundação Carlos Chagas Filho de Amparo à Pesquisa do Estado do Rio de Janeiro, Conselho Nacional de Desenvolvimento Científico e Tecnológico and the Ministério da Ciência, Tecnologia e Inovacão, the Deutsche Forschungsgemeinschaft, and the Collaborating Institutions in the Dark Energy Survey. The Collaborating Institutions are Argonne National Laboratory, the University of California at Santa Cruz, the University of Cambridge, Centro de Investigaciones Enérgeticas, Medioambientales y Tecnológicas-Madrid, the University of Chicago, University College London, the DES-Brazil Consortium, the University of Edinburgh, the Eidgenössische Technische Hochschule (ETH) Zürich, Fermi National Accelerator Laboratory, the University of Illinois at Urbana-Champaign, the Institut de Ciències de l'Espai (IEEC/CSIC), the Institut de Física d'Altes Energies, Lawrence Berkeley National Laboratory, the Ludwig-Maximilians Universität München and the associated Excellence Cluster Universe, the University of Michigan, the National Optical Astronomy Observatory, the University of Nottingham, the Ohio State University, the OzDES Membership Consortium, the University of Pennsylvania, the University of Portsmouth, SLAC National Accelerator Laboratory, Stanford University, the University of Sussex, and Texas A&M University.

Based on observations at CTIO, National Optical Astronomy Observatory, which is operated by the Association of Universities for Research in Astronomy (AURA) under a cooperative agreement with the National Science Foundation.

This research used the facilities of the Canadian Astronomy Data Centre operated by the National Research Council of Canada with the support of the Canadian Space Agency. This research has made use of the NASA/IPAC Extragalactic Database (NED) which is operated by the Jet Propulsion Laboratory, California Institute of Technology, under contract with the National Aeronautics and Space Administration.

REFERENCES

Amorisco N. C., Zavala J., de Boer T. J. L., 2014, ApJ, 782, L39
Antilogus P., Astier P., Doherty P., Guyonnet A., Regnault N., 2014, J. Instrum., 9, C03048
Aparicio A., Gallart C., 1995, AJ, 110, 2105
Aparicio A., Gallart C., 2004, AJ, 128, 1465
Aparicio A., Hidalgo S. L., 2009, AJ, 138, 558
Aparicio A., et al., 2016, ApJ, 823, 9
Battaglia G., Helmi A., Tolstoy E., Irwin M., Hill V., Jablonka P., 2008, ApJ, 681, L13
Battaglia G., Irwin M., Tolstoy E., Hill V., Helmi A., Letarte B., Jablonka P., 2008, MNRAS, 383, 183
Becker R. H., et al., 2001, AJ, 122, 2850
Bettinelli M., Hidalgo S. L., Cassisi S., Aparicio A., Piotto G., 2018, MNRAS, 476, 71
Bouchard A., Carignan C., Mashchenko S., 2003, AJ, 126, 1295
Carignan C., Beaulieu S., Côté S., Demers S., Mateo M., 1998, AJ, 116, 1690
Castelli F., Kurucz R. L., 1993, in Dworetsky M. M., Castelli F., Faraggiana R., eds, IAU Colloq. 138: Peculiar versus Normal Phenomena in A-type and Related Stars, Vol. 44. Astron. Soc. Pac., San Francisco, p. 496
Coleman M. G., Da Costa G. S., Bland-Hawthorn J., 2005, AJ, 130, 1065
Da Costa G. S., 1984, ApJ, 285, 483
de Boer T. J. L., et al., 2011, A&A, 528, A119
de Boer T. J. L., et al., 2012, A&A, 539, A103
de Vaucouleurs G., de Vaucouleurs A., Corwin H. G., Jr., Buta R. J., Paturel G., Fouqué P., 1991, Third Reference Catalogue of Bright Galaxies. Springer-Verlag, Berlin
Flaugher B., et al., 2015, AJ, 150, 150
Gallagher J. S., III, Wyse R. F. G., 1994, PASP, 106, 1225
Helmi A., et al., 2006, ApJ, 651, L121
Hidalgo S. L., et al., 2011, ApJ, 730, 14
Hidalgo S. L., et al., 2013, ApJ, 778, 103
Hurley-Keller D., Mateo M., Grebel E. K., 1999, ApJ, 523, L25
Irwin M., Hatzidimitriou D., 1995, MNRAS, 277, 1354
Ivezić Ž., , et al., 2007, AJ, 134, 973
Kirby E. N., Guhathakurta P., Bolte M., Sneden C., Geha M. C., 2009, ApJ, 705, 328
Kirby E. N., Lanfranchi G. A., Simon J. D., Cohen J. G., Guhathakurta P., 2011, ApJ, 727, 78
Kroupa P., 2002, Science, 295, 82
Leitherer C., et al., 1999, ApJS, 123, 3
Łokas E. L., 2009, MNRAS, 394, L102
Mac Low M.-M., Ferrara A., 1999, ApJ, 513, 142
Mapelli M., Ripamonti E., Battaglia G., Tolstoy E., Irwin M. J., Moore B., Sigurdsson S., 2009, MNRAS, 396, 1771
Martínez-Vázquez C. E., et al., 2016, MNRAS, 461, L41
McConnachie A. W., 2012, AJ, 144, 4
Menzies J. W., Feast M. W., Whitelock P. A., Matsunaga N., 2011, MNRAS, 414, 3492
Monelli M., et al., 2012, ApJ, 744, 157
Monkiewicz J., et al., 1999, PASP, 111, 1392
Piatek S., Pryor C., Bristow P., Olszewski E. W., Harris H. C., Mateo M., Minniti D., Tinney C. G., 2006, AJ, 131, 1445
Pietrinferni A., Cassisi S., Salaris M., Castelli F., 2004, ApJ, 612, 168
Pietrzyński G., et al., 2008, AJ, 135, 1993
Queloz D., Dubath P., Pasquini L., 1995, A&A, 300, 31
Ricotti M., Gnedin N. Y., 2005, ApJ, 629, 259

Salaris M., Cassisi S., 2005, Evolution of Stars and Stellar Populations. Wiley-VCH, New York, p. 400
Schlafly E. F., Finkbeiner D. P., 2011, ApJ, 737, 103
Schlegel D. J., Finkbeiner D. P., Davis M., 1998, ApJ, 500, 525
Seaman R. L., De La Pena M., Zarate N., Lauer T. R., 2002, Proc. SPIE, 4846, 182
Shapley H., 1938, Harv. Coll. Obser. Bull., 908, 1
Stetson P. B., 1993, in Butler C. J., Elliott I., eds, IAU Colloq. 136: Stellar Photometry – Current Techniques and Future Developments. Cambridge University Press, Cambridge, p. 291
Stetson P. B., Davis L. E., Crabtree D. R., 1990, CCDs Astron., 8, 289
Tolstoy E., , et al., 2004, ApJ, 617, L119
Tolstoy E., Hill V., Tosi M., 2009, ARA&A, 47, 371
Valdes F., Gruendl R., DES Project, 2014, in Manset N., Forshay P., eds, ASP Conf. Ser., Vol. 485, Astronomical Data Analysis Software and Systems XXIII. Astron. Soc. Pac., San Francisco, p. 379
van den Bergh S., 1999, A&AR, 9, 273
Westfall K. B., Majewski S. R., Ostheimer J. C., Frinchaboy P. M., Kunkel W. E., Patterson R. J., Link R., 2006, AJ, 131, 375

This paper has been typeset from a TEX/LATEX file prepared by the author.